METEOROIDS: NEEDS FOR PENETRATION SCALING LAWS

AND THE POTENTIALS OF SIMULATION TECHNIQUES

By E. T. Kruszewski

NASA Langley Research Center
Langley Station, Hampton, Va.

METEOROIDS: NEEDS FOR PENETRATION SCALING LAWS

AND THE POTENTIALS OF SIMULATION TECHNIQUES

By E. T. Kruszewski
Langley Research Center

INTRODUCTION

Meteoroids are celestial bodies traveling at velocities ranging from 35,000 to 200,000 feet per second. They range in size from the smallest dust particle to large boulders. Fortunately, the larger the size the less frequent is its occurrence. The larger micrometeoroids because of their great speed could completely penetrate a space vehicle wall while the more numerous dust size particles could bombard and erode reflective surfaces, ports, lenses, and any other exposed apparatus that relies on its surface properties for proper operation.

Consequently there are two general areas that are of interest to the space technologist: Penetration by individual hypervelocity particles of the larger size that could penetrate walls of space vehicles and the erosion effects caused by the scrubbing action of the more numerous smaller particles.

LOW-VELOCITY IMPACTS

Empirical Scaling Laws

Even before space flight and its accompanying meteoroid problem there was interest in penetration phenomena and high-velocity particle accelerators for the purpose of studying armor penetration. The bulk of these investigations, however, had to do with cratering phenomena below 15,000 feet per second and resulted in empirical formulas for penetration based on best fit curves through experimental data. Some of the most widely used empirical formulas were based on correlation of experimental data with an empirical formula of the form

$$\frac{p}{l} = K\rho_p^m V^n \tag{1}$$

where

p   penetration

l some reference dimension of the projectile

ρ_p density of the projectile
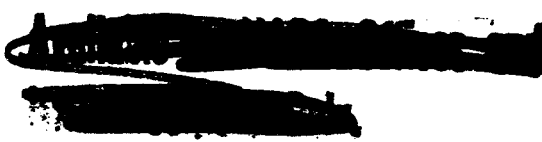
V   impact velocity

K   proportionality constant

Experiments were performed using various target and projectile materials, various shapes of projectiles, and covering different velocity ranges. Each experimentalist found the value of m and n that best fitted his experimental data usually disregarding the experimental data of others. Thus values of m from 1/3 to 1 and of n from 1/3 to 1.4 were recommended.

Other empirical relationships can be derived from the simple equation of motion shown in equation (2).

$$\frac{\pi}{6} \rho_p d^3 u \cdot du = -F dp \tag{2}$$

where ρ_p is the density of the projectile; d, the diameter; u, the instantaneous velocity; p, the penetration; and F, the resistive force. This expression equates the change in kinetic energy to the work done by the resistive force F on the projectile. Thus, the form of the penetration equation is automatically dictated by the assumption of a resistive force. Conversely, any assumed penetration formula implicitly implies a resisting force.

Shown in figure 1 are a few of the possible expressions for resistive force and the resulting penetration formula.

If the resistive force is assumed to be dependent only on the presented area of the projectile, that is, equal to some constant k, the penetration formula is of the form $\rho_p V^2$. If free surface effects are taken into account by assuming that the force is dependent on the depth of penetration (see eq. (2) of fig. 1), the penetration is of the form $\rho_p^{1/2} V$. Assuming a stronger dependence of the resistive force on the penetration (see eq. (3) of fig. 1), a formula with penetration proportional to $\rho_p^{1/3} V^{2/3}$ is obtained.

This and the next two formulas in figure 1 are of special interest as they are the most widely used and were originally obtained by relating the crater volume to either the kinetic energy or momentum of the particle.

The V to the 2/3 power penetration formula corresponds to the assumption that crater volume is proportional to kinetic energy of the projectile. The V to the 1/3 power formula corresponds to the assumption that crater volume is proportional to momentum of the projectile, while the V to the unit power states that crater volume is proportional to momentum per unit area of the projectile.

Notice from equations 4 and 5 of figure 1 that the momentum formula corresponds to a resistive force that increases with increasing impact velocity

2

while the momentum per unit area formula results in a resistive force which decreases with increasing impact velocity.

If the resistive force is assumed proportional to the inertial forces created in the target $\left(\rho_t V^2\right)$, the resultant penetration formula has a logarithmic dependence with respect to the velocity. (See eq. (6) of fig. 1.) If a term independent of velocity is added to allow for the effect of material properties such as strength, hardness, etc., the penetration formula is also of the logarithmic form.

All of these forms of the penetration equation, except the first and second, have been advocated by at least one of the numerous experimentalists in the hypervelocity penetration field.

Theoretical Scaling Laws

One of the earliest attempts to predict penetrations by a theoretical analysis occurred when E. M. Pugh and several other investigators (ref. 1) attempted to predict penetrations produced by a shaped-charge jet. The penetration model which was used is shown in figure 2.

The projectile was considered to be a jet of incompressible fluid of length l. The jet impinged on the target which was also considered to be an incompressible fluid. On the left side of the figure is shown the penetration process as viewed from the rest or laboratory frame of reference. V is the jet velocity; ρ_p and ρ_t, the jet and target densities; p, the penetration; and u is the velocity of the penetrating projectile material.

The penetration process as viewed from a moving reference frame originating at the bottom of the crater is shown on the right side of figure 2. The velocity of the material inside the jet is V-u, while the velocity of the target material is u.

In this reference frame the flow can be considered to be steady. The stagnation pressure in both the target and projectile region can then be obtained by the Bernoulli's equation. As the stagnation pressure in both regions may be the same, a relationship between u and V can be derived and the resulting penetration at u = 0 can be written as

$$\frac{p}{l} = \sqrt{\frac{\rho_p}{\rho_t}}\left[\frac{1 - \sqrt{\frac{\rho_t}{\rho_p}\left[1 - \left(\frac{V_o}{V}\right)^2\left(1 - \frac{\rho_p}{\rho_t}\right)\right]}}{\sqrt{1 - \left(\frac{V_o}{V}\right)^2\left(1 - \frac{\rho_p}{\rho_t}\right)} - \sqrt{\frac{\rho_t}{\rho_p}}}\right] \tag{3}$$

3

where l is the length of the projectile and V_0 is the minimum velocity that will first cause a crater. This parameter was empirically introduced into the Bernoulli's equation of target material in an attempt to introduce the effects of strength of the target material.

When the target and projectile materials are the same, the equation simplifies to the simple expression

$$\frac{p}{l} = \frac{1 - \left(\frac{V_0}{V}\right)^2}{1 + \left(\frac{V_0}{V}\right)^2} \tag{4}$$

This equation was very successful in predicting the penetration of jets and of long narrow projectiles at relatively low velocities; for higher velocities, however, this equation gave rather questionable results and for velocities much greater than V_0 the penetration formula becomes independent of the impact velocity $\left(\frac{p}{l} = 1\right)$.

In order to remedy this fault a more refined model shown in figure 3 was suggested by Öpik.

The projectile was taken to be a circular cylinder of radius r_0 and length $2r_0$. An allowance for the yield strength of the target material was made through the use of a strength parameter k, which is defined as the minimum pressure at which a penetration can occur.

As in the preceding model, both the projectile and target are considered to be incompressible fluids. The flow pattern after impact is shown in the right. As the projectile strikes the target it is decelerated by the resistance of the target in the form of the pressure p. This resistance creates a velocity gradient in the projectile material and results in a radial displacement r and radial motion of the projectile material $\dot{r}$.

By the use of the conservation of mass of the projectile, Bernoulli's equations for both the projectile and target materials, and an equation of motion, the maximum displacement was found, in terms of a complicated integral, which was indeed a function of impact velocity. A comparison of the results of Öpik's model and the jet equation by Pugh will be shown a little later in the paper.

4

METEOROID VELOCITY IMPACTS

Empirical Formulas

When the need for information dealing with the interaction of meteoroids and materials first became apparent, the logical step for the spacecraft designer was to turn to armor penetration analysis for his formulas. The danger of such a procedure can be seen from an examination of figure 4.

Plotted in this figure is the nondimensional penetration p/l as a function of velocity in thousands of feet per second for four of the best known empirical penetration formulas: the momentum per unit area formula, the kinetic energy formula, the formula based on momentum, and finally the logarithmic form of the penetration formula which was based on an inertia resistive force.

To restrict comparisons to the effects of impact velocity, the projectile and target material were taken to be the same. For the sake of comparison, the constant K for all formulas was chosen so that a penetration of 0.1 was obtained at a velocity of 15,000 feet per second.

The danger of using any of these formulas to predict penetrations of particles at a high meteoroid velocity, which is one order of magnitude greater than the maximum experimental velocity, is obvious from this figure. Differences in predicted penetration of one order of magnitude can be had, depending on the formula used. This uncertainty in penetration prediction can not be tolerated.

Even if the penetration relationship at the lower velocities was known, it still would be dangerous to extrapolate to higher velocities. This is due to the fact that the mechanism of penetration is so dependent on impact velocity. This dependence is demonstrated in figure 5.

Shown in this figure are the results of an experimental investigation in which steel and tungsten carbide particles were impacted into soft lead. (See ref. 2.) The results separate into three individual regions depending on the condition of the projectile after impact. In region I the projectile remains intact and the penetration increases with velocity to the 4/3 power. The crater shape is long and narrow with about the same cross section as the projectile. As the velocity is increased the projectile starts to deform and the crater becomes wider. In region II the penetration actually decreases with velocity, while the crater tends to become spherical. In region III the projectile reaches the fluid state and the penetration increases as V to the 2/3 power.

Hypervelocity Penetration Mechanism

A qualitative description of what happens to a semi-infinite target when impacted at meteoroid velocities can be described with the aid of figure 6.

The top sketch of figure 6 shows the projectile just before impact. The particle is assumed to be traveling at speeds well above the speed of sound in the target material (for example, the speed of sound in steel is about 17,000 feet per second). The target is considered to be a semi-infinite body.

Immediately after impact there is an intense light flash. Shock waves are propagated into the target and into the projectile. If the velocity of impact is high enough, both shock waves travel into the target. Small fragmentary particles, some of which travel at about twice the speed of impact, are ejected from the target surface.

A short time later the shock waves have propagated into both the target and projectile. The pressures and temperatures across the shocks, which depend on the impact velocity, are so great that the target material can be considered a fluid with negligible load-carrying ability. The projectile material on the other side of the shock, of course, is not as yet aware of the impact and so continues to penetrate the target. This downward motion of the projectile imparts an outward motion of the fluid particles causing the fluid material to erupt out of the target thus forming a crater and lip. Meanwhile an expansion wave, traveling at a velocity higher than the shock velocity, originates from the corner of the projectile and is propagated into the target material. This expansion wave relieves the highly compressed material within the shocked region.

Eventually the expansion catches up with the shock. Thus the shock is weakened to the point where the temperatures across the shock are below those necessary to melt the target material and the pressures approach their allow-able dynamic stresses. At this time further penetration continues through the propagation of plastic and elastic stress waves resulting in a mechanical cratering process.

Thus the energy of a hypervelocity projectile is dissipated by a variety of mechanisms: A flash or explosion, melting and vaporization of both target and projectile material, resistance of the target as a fluid mass, and plastic and elastic deformation and snapback.

A feeling for the order of magnitude of the pressures, densities, and tem-peratures associated with such shock phenomena can be had by examining the one-dimensional case of impact shown in figure 7.

On the left side of this figure is shown a one-dimensional body traveling at a velocity V and density ρ_0 just prior to impacting a stationary one-dimensional body. The density of the target material is the same as that of the projectile (i.e., ρ_0). The two bodies after impact are shown on the right side of figure 7.

The velocity of the interface between the particle and target is equal to one-half of the impact velocity. The velocity of the shock front into the tar-get is, of course, always greater than this, as the density of the shocked material is always increased.

The motion of the rear shock can be in either direction depending on the density ratio. If the material between the shocks is compressed to more than twice its original density $\left(\rho_1/\rho_0 > 2\right)$ the shock will travel into the target.

If not, the shock will travel into the projectile. The value of this density ratio and the resulting pressures are shown in figure 8.

In this figure a plot of the density ratio ρ/ρ_0 and resulting pressure in the shocked region is shown as a function of the impact velocity in feet per second plotted on a log scale. The velocity in kilometers per second is shown on the bottom scale. These results are for iron impacting on iron and were obtained from some experimental work done at Los Alamos. (See ref. 3.) Note that for iron a density ratio of 2 occurs at an impact velocity of about 70,000 feet per second. Thus at this impact velocity the rear shock wave will remain stationary at the impact surface.

The pressures resulting from these density ratios are shown by the pressure curve. Note that the pressures are plotted in megabars, where 1 megabar is approximately equal to 14.7 million psi. Notice also that even for impact velocities below 20,000 feet per second pressures in the range of 20 to 30 million psi will be generated. At 200,000 feet per second, the maximum estimated meteoroid velocity, the pressures reach over 30 megabars (450 million psi). The temperatures at these high pressures are in the thousands of degrees, which are well above the melting and even the vaporization temperature of the material.

Although the one-dimensional solution permits us to evaluate the pressures and density change across the shock, it does not contain a mechanism for dissipation of the shock nor crater production. Consequently, no estimate of penetration can be obtained through its use.

Early Theoretical Approaches

Many theoretical approaches for the prediction of high-velocity cratering phenomena have been used. The results of three of the earliest attempts to predict penetration are shown in figure 9. Each of these theoretical approaches assumes that the crater is formed by a different cratering mechanisms.

The thermal penetration theory (first suggested by Whipple) assumes that the craters are formed by removal of the target material by melting or vaporization. Consequently, the crater volume is obtained by dividing the energy of the projectile by the energy necessary to melt a unit volume of target material. The penetration equation is of the form shown at the top of figure 9 where K is a constant depending on the shape of the projectile and crater and Q is the energy necessary to melt a unit mass of target material. The explosive penetration theory (see ref. 4) assumes that the crater is identical to that formed by an amount of explosive whose energy is equivalent to the kinetic energy of the projectile. The explosive is assumed to generate a powerful shock wave that converts all of the target material to a strongly compressed polytropic gas. The cratering process is assumed to continue until the energy

on the shock front is less than the internal energy required to disintegrate the target material. The penetration equation for this case is identical in form to the thermal penetration analogy. In this equation (see fig. 9) R represents the energy required to disintegrate the target material and K depends on the material properties of the target.

Grimminger (ref. 5) presented the first theory based on the hydrodynamic analogy which assumes that the target is a compressible fluid. This assumption is suggested by the extremely large pressures generated in high-velocity impact. As the material strength is small in comparison to these pressures, it can be neglected. Grimminger's analyses assumed that the projectile was a rigid sphere and that the penetration occurred in two phases. In the first phase the projectile was decelerated by the drag force exerted by the compressible fluid on the projectile. This deceleration continued until the projectile reached a speed of Mach 5. The final penetration was assumed to be given by an empirical penetration formula derived from armor penetration at low velocities. The resulting penetration formula is shown at the bottom of figure 9. The first term of this formula is that due to the drag force while the second is the empirical armor penetration equation.

Hydrodynamic Approach

One of the most complete and detailed solutions of hypervelocity penetration was based on the hydrodynamic analogy. The problem solved was that of a cylindrical projectile of length equal to its diameter and made of the same material as the target. Both the target and projectile are considered to be compressible inviscid fluids. The analysis is based on a solution of the nonlinear compressible fluid equations shown below.

$$
\left.
\begin{aligned}
&\rho \, \frac{\partial \vec{u}}{\partial t} + \left(\rho \vec{u} \cdot \nabla\right)\vec{u} + \nabla p = 0 \\[2ex]
&\frac{\partial \rho}{\partial t} + \vec{u} \cdot \nabla \rho + \rho \nabla \cdot \vec{u} = 0 \\[2ex]
&\rho \, \frac{\partial e}{\partial t} + \rho \vec{u} \cdot \nabla e + p \nabla \cdot \vec{u} = 0 \\[2ex]
&P = f(\rho, e)
\end{aligned}
\right\} \tag{5}
$$

where u is the fluid particle velocity; p, the pressure; e, the specific internal energy; and ρ, the density.

These equations represent the conservation of momentum, conservation of mass, the energy equation, and the equation of state. Note that viscosity and heat-conduction terms are neglected. The equation of state used was the so-called Los Alamos equation of state for metals. This equation was obtained by means of interpolating between results of an experimental Hugoniot in the low

8

megabar pressure range and an analytical equation of state using the Fermi-Thomas-Dirac theory for material in the higher pressure range.

These fluid equations had to be solved numerically. The numerical method used was the one referred to as the "Particle In Cell" or PIC method and is discussed in reference 6.

In this method the region of interest is divided into a finite number of computational cells which are fixed relative to the observer. Each cell has a velocity, internal energy, and total mass associated with itself. The fluid is represented by individual particles or mass points which move through this Eulerian mesh in Lagrangian fashion. In the solution, these equations are written in finite difference form and then solved explicity.

The results of such an analysis are shown in figures 10 through 12.

In figure 10 are shown the pressure contours and velocities at $3\frac{1}{2}$ seconds after the impact of an iron projectile on an iron target. The projectile was assumed to have been traveling at 18,000 feet per second.

The vectors indicate the direction and magnitude of the velocity at each mesh point located at the tail of the vector. The contour lines are isobars representing equal pressures of 2, 1, and 0.2 megabars. The cylindrical projectile had a 10-centimeter diameter and a 10-centimeter height.

Note that there are two pressure pulses of more than 2 megabars and that the pressures throughout the affected region are in the megabar range. One pulse is traveling into the target and the other into the projectile. Notice also that the numerical method used does not retain the discontinuity of the shock. Instead the shocks are smeared over a wide area.

The velocities of all target points beyond 0.2-megabar contour are zero thereby indicating that the points have not, as yet, felt the impact. Similarly the velocity of the projectile points above the 0.2-megabar contour are equal to the initial velocity and thus are not aware that the front of the projectile is being stopped. Note that the velocity vectors near the axis of symmetry are parallel to the initial projectile velocity. This is an indication that these points are still not aware that the projectile is finite. The finiteness of the projectile is indicated by the generation of an expansion wave from its outer circumferential points. Consequently, all of these points act as in the one-dimensional case.

The pressures and velocities at 8.7μ sec after impact are shown in figure 11. From this figure it can be seen that the rarefraction wave has now reached the line of symmetry and has also caught up with the shock wave. All pressures are still relatively high. The pressure at the shock, which has been weakened by the expansion wave and by the fact that it is encompassing more volume, is now only 1.0 megabar at its maximum.

In figure 12 the pressures and velocities at 81.7μ sec are shown. At this point the shock is spherical and has just about dissipated itself. Now all the pressures are relatively low. The maximum pressures are only 0.1 megabar.

Two investigators have used this method of analyses to determine dependence of penetration on velocity (R. J. Bjork ref. 3 and J. W. Walsh ref. 7). Bjork's investigation, from which the data for the preceding figures were taken, was published in 1959 while Walsh's investigation was reported in 1963.

Both have claimed to use identical methods for calculating the pressure, velocity, and density distributions and the same equation of state. They have, however, come up with entirely different conclusions.

Bjork continued his analysis until the shock wave was dissipated, such as is shown in figure 12. He then defined his penetration by using the points of zero pressure to define the crater boundary. Using this crater criterion he made calculations for impacts with both aluminum and iron at three different velocities. The results of these calculations are shown in figure 13.

Plotted in this figure is the nondimensional penetration p/d as a function of velocity on a log-log scale. The triangles represent the results for aluminum while the circles are for iron.

The straight line drawn through these points has a slope of $V^{1/3}$. Thus Bjork concluded that the crater volume is dependent on the momentum of the particle (at least for the hypervelocity impact region).

Walsh's arguments (ref. 6) were as follows:

In the early stages of projectile-target interaction, pressures and temperatures throughout the affected region are indeed sufficiently high to neglect strength properties and the hydrodynamic approach is applicable. On the other hand, in the later states of penetration the pressures are comparable to the ultimate or yield strength of the material. Consequently, the penetration cannot be considered a totally hydrodynamic problem.

Recognizing this, Walsh did not calculate crater sizes. Instead he attempted to treat only that portion of the penetrator that is formed during the high-pressure phase of the penetration phenomena. In doing this Walsh postulated that, if at any time during the formation of craters resulting from different impacts the pressure pulses and velocities were the same, then the subsequent reaction of the target material should be the same.

Making use of this principle, Walsh calculated the pressure and velocity distribution for a number of impacts of iron cylinders and iron targets. In all cases he varied the mass and velocity of the projectile while keeping the kinetic energy constant. From comparisons of pressure and velocity plots he concluded that the hydrodynamic portion of the penetration process varies as $V^{0.62}$. This is approximately $V^{2/3}$ which states that crater volume depends on kinetic energy.

10

To summarize the results of the theoretical approaches, calculations were made of the penetration of an iron projectile into an iron target using the theoretical approaches just discussed. The results are shown in figure 14.

Curves are shown for the jet penetration mode, Öpik's, Grimminger's equation, and the curves resulting from Bjork's and Walsh's investigations. The thermal and explosive analogy curves would, of course, be parallel to the $V^{2/3}$ curve. There is some experimental work at 25,000 feet per second that lies between the $V^{1/3}$ and $V^{2/3}$ work. From this we could conclude that the incompressible fluid models of Pugh and Öpik are not applicable to the hypervelocity range. Even with this, however, the spread of the predicted penetration in the high meteoroid velocity range is still too great for design purposes.

Even the results of the two most exact analyses differ considerably in the higher impact velocity range. This is in spite of the fact that they used identical approaches, and differed only in their criteria of crater formation.

METEOROID SIMULATION TECHNIQUES

Concurrent with the development of theoretical approaches, there has been an increasing effort to improve existing accelerators to meet the need for meteoroid simulation.

There are three requirements that must be met for the accurate simulation of the meteoroid environment:

First, the technique should be capable of obtaining impact velocities in the meteoroid velocity range (i.e., between 35,000 and 200,000 ft/sec).

Second, the technique should be such that the mass, size, and velocity of the projectile are either known or can be accurately measured.

Finally, the technique should be capable of accelerating a large number of smaller particles. This requirement is, of course, not needed for studying the penetration damage done by the large micrometeoroids. It is, however, needed to investigate the erosion damage done by the more numerous smaller micrometeoroids.

Accelerators For Armor Penetration

Two of the methods that were extensively used for armor penetration investigations are the light-gas guns and the explosive charge accelerators. The light-gas gun consists of two stages: a pump tube and a launch tube separated by a diaphragm. The pump tube consists of a light gas and a piston device to compress the gas. When the pressure becomes large the diaphragm is ruptured allowing the pressurized gas to accelerate the projectile down the launch tube.

The velocities obtained from these devices, however, were well below meteoroid velocities. Some of the methods used to increase their velocity capabilities are shown in figure 15.

The top sketch shows the basic scheme of staging. In this system the projectile of the first gun acts as a piston for the second.

The velocity of a light-gas gun is dependent on the ratio of the gas temperature to the mass of the gas. As the mass of the gas is already a minimum, higher velocities can be obtained only through raising the temperature of the gas. Three schemes have been used to augment the energy of the gas: electrical discharge into the gas, preheating the pump tube before injecting the gas, and preheating the gas outside and injecting it into the pump tank just prior to compression. Another approach to increasing the efficiency of light-gas guns has to do with proper design of the transition section. On the bottom left of figure 15 is an aerodynamic throat transition section which was designed to provide minimum resistance to gas passage. On the right is the accelerated breech transition section. In this design a piston of low mechanical strength extrudes itself into a very small angle conical transition. This extruding action creates an increase in the velocity and pressure of the front face of the piston.

A summary of the maximum capabilities of present light-gas gun facilities is shown in figure 16.

Shown in this figure is the maximum velocity in feet per second as a function of the projectile weight in grams. Equivalent velocities in kilometers per second are shown on the right-hand scale.

The circles represent the velocities of guns using the tapered throat and powder accelerated pistons. The square symbols represent the guns using aerodynamic throats. The numerals above the square symbols denote which pump tube configuration was used.

Note that the highest velocity obtained with a light-gas gun is about 34,000 ft/sec, which is still below even the minimum meteoroid velocity. Furthermore, at this velocity only one or two shots can be obtained before the guns must be rebored.

Some of the methods developed for increasing the efficiency of the explosive charge techniques, also used initially in armor penetration, are shown in figure 17.

The top sketch is an illustration of the so-called cavity charge technique. In this technique the detonation wave propagates through the explosive until it reaches the cavity wall. At this time it generates a strong shock wave which is propagated through the cavity. The detonation wave continues through the walls of the tubular section of the explosive at a higher velocity than the original shock wave in the cavity. This detonation wave, in turn, generates other shocks from the inner sidewalls. These additional shocks interact with the original shock, progressively compressing it and creating a

12

corresponding increase in peak pressure. Such devices have accelerated particles up to 25,000 ft/sec.

Another approach to the shaped-charge techniques are the linear charges shown in the bottom two sketches of figure 17. In this technique the projectile is formed during the launch stage.

As the detonation wave progresses forward, it collapses the metal liner material onto the axis and forms the projectile. Velocities as high as 67,000 feet per second have been measured for the cylindrical liner while a velocity of 49,000 feet per second has been obtained with the conical liner. The disadvantage of this technique is that neither the shape nor mass of the projectile is accurately known.

Accelerators For Meteoroid Simulation

Neither the light-gas gun nor shaped-charge accelerators meet the requirements for simulation of true meteoroid environment. The velocity of the light-gas gun is too low and the particle size of the explosive charge technique is not accurately known. Consequently, in the last few years there has been an increase in effort to develop entirely new acceleration techniques. Two of the most promising are the exploding wire or foil guns and the electrostatic accelerators.

An exploding foil gun is shown schematically in figure 18. It consists of a bank of capacitors connected through a switch to a thin aluminum foil of 1/4-mil thickness. The two solid plastic blocks approximately 2 inches square and one-half inch thick act as a breech and a plastic tube acts as an expandable barrel. The barrel is then mounted into a vacuum chamber that also houses the target.

The exploding foil gun utilizes the explosive force achieved by abruptly discharging the large quantity of electrical energy stored in the capacitors through the thin metal film. When this discharge occurs the film is heated to a molten state in a relatively short time (less than a millisecond). The inertia of the film holds it in place until it becomes superheated and explodes. The explosive force punches a disk-shaped particle which forms the projectile. The projectile sizes can be altered by changing the diameter of the tube and the thickness of the diaphragm. Projectile material can be altered by using different material diaphragms. Barrels ranging from 1/8 to 1/2 inch in diameter and disk thicknesses from 0.002 inch to 0.050 inch have been successfully used.

A sequence of pictures of the firing of an exploding foil gun is shown in figure 19. The pictures were taken at 10-, 25-, 28-, and 30-second intervals after the closing of the switch.

It takes about 10 seconds for the diaphragm to shear, allowing the plasma and the projectile to be accelerated down the barrel. At 25μ sec the projectile is well down the barrel. At 28μ sec the projectile is out of the barrel and almost impacting the target. You can see the shock wave ahead of the

projectile just beginning to be reflected by the target. The last picture shows the projectile impacting the target with the accompanying spray of particles. Two interesting points are brought out by these pictures: First, the plasma front is always ahead of the projectile; and, second, the barrel and breech remain intact until the particle is well on its way. As of today this technique is in its development stage. Exploding foil guns have accelerated 10-mg particles to about 35,000 feet per second with only 6000 joules of electrical energy. This indicates only a 5-percent efficiency of converting electrical energy into kinetic energy of the particle.

Analyses and experimental investigations are under way at Langley and several other organizations to improve this efficiency.

Some of the improvements needed for better efficiency are:

1. More available energy

2. Higher voltage on capacitors

3. Maximum rate of current rise

4. Lowest possible inductance

5. Better and lower induction switching

Another version of the electrical discharge accelerator is the exploding wire gun developed by Mr. Scully of North American Aviation. The facility utilizes the discharge of a large bank of capacitors of about 40,000 joules but, instead of a plastic barrel and breech and aluminum foil, it utilizes a lithium wire arc chamber shown in figure 20.

The arc chamber consists of an insulated lithium wire attached to the capacitor at one end and to ground at the launch tube end. The projectiles are placed on a carrier membrane at the entrance to the launch tube. The membrane is in contact with the arc chamber electrode. The particles consist of thousands of small glass spheres ranging in size from 10 to 50 microns in diameter. Upon discharge of the capacitors the particles are accelerated by the lithium plasma down the launch tube which is evacuated to a pressure of 3 to 7 microns of mercury. Baffle plates are used to prevent all but a few particles from striking the target. The maximum velocity achieved with this device is about 60,000 feet per second with a 50-micron particle.

The other technique which has the potential of simulating the meteoroid environment is the electrostatic accelerator. This technique has the potential of reaching the highest meteoroid velocity. This method is applicable only to the smaller particles but allows for the acceleration of a stream of particles to meteoroid velocities thereby permitting a study not only of penetration but also of erosion effects of micrometeoroids.

The interest in this facility stems from the range of velocities that is attainable from consideration of the equations

14

$$v = \sqrt{\frac{2Vq}{m}} \qquad\qquad (6a)$$

$$v = K\sqrt{\frac{VE}{r\rho}} \qquad\qquad (6b)$$

Equation (6a) shows the velocity attained by a particle of mass m with a charge q exposed to an electrical potential V. The charge on a particle can be expressed in terms of the surface field strength on the particle E. Hence the velocity of a spherical charged particle can be related to its radius r, density ρ, voltage V, and surface field strength E, as shown in equation (6b).

This form of the equation is preferred as the maximum charge which a particle can retain can be expressed in terms of this parameter E. The maximum value of E is determined by the ability of the material to hold electrons or ions and is about one order of magnitude greater for a positive charge than for a negative charge. Consequently, only positively charged particles are considered for electrostatic acceleration.

The significance of this equation is shown in figure 21 where the attainable velocities for an iron particle, one micron in diameter, are plotted as a function of voltage in millions of volts. The curves are drawn for the maximum theoretical charge possible (which is 2.0×10^{10} volts/meter), 50 percent of maximum, and a charge corresponding to about 12 percent of the maximum or 2.5×10^9 volts/meter.

This lower value represents the charge that can be placed on a particle by the only fully developed charging device. In this device the particles to be charged are allowed to come into contact with a small spherical charging electrode which is maintained at a high positive voltage. In the original accelerator this charging device was mounted on the accelerator tube in the dome of a two-million-volt Van de Graaff generator. Thus a micron-size particle would be accelerated to about 28,000 feet per second. Smaller particles, of course, would reach higher speeds. At the present time Langley is installing a similar device but is using a 4-million-volt Van de Graaff generator which is the largest horizontal machine made. Thus with this device we can achieve about 40,000 feet per second with a 1-micron-size particle.

As can be seen from these curves, velocities in the 100,000-feet-per-second range can be realized either by improving the particle charging device or by providing larger accelerating voltages. Both of these approaches are being investigated.

In the light of recent developments the most attractive approach to obtaining the higher velocities is through an increase in voltage. Theoretical studies have shown that voltages of the order of 20 to 30 million volts are entirely feasible by the use of a linear accelerator such as shown in figure 22.

Devices similar to this have been used by nuclear physicists to accelerate electrons and protons. It consists of a linear array of cylindrical draft tubes of which the length and gap separation progressively increase. Alternating tubes are connected to opposite terminals of an alternating-current source. The frequency of this source is adjusted so that each time the particle enters a gap it sees an accelerating voltage. Consequently, the total accelerating voltage is equal to the sum of all the accelerations received at each gap.

Studies are also under way to improve the charging devices. One promising new method is one that charges the particles by exposing them to a concentrated ion beam. One such method (see ref. 9) has successfully imposed a large charge on carbon particles. However, it takes from 4 to 8 hours to charge just one small particle. In addition, the charging device requires constant visual observation of the particle precluding its integration into a Van de Graaff accelerator.

A summary of the meteoroid simulation capabilities is shown in figure 23 where the attainable velocity in both feet per second and kilometers per second is plotted against the size of the projectile in meters. The solid lines indicate present capabilities of these devices while the dotted lines are realistic potentials for the near future. The shaded area represents the estimated meteoroid velocity range. As the figure illustrates, the existing devices are capable of simulating the meteoroid impacts only in the lower meteoroid velocity region. In the near future, however, velocities in the higher meteoroid velocity region will be possible with the electrostatic accelerator. This, of course, will be with the smaller, dust size particles. Larger particles can be accelerated only to about 60,000 feet per second even with the anticipated improvement in the exploding foil gun.

Of all these devices the electrostatic accelerator is the only one that can accelerate the high fluxes of particles needed (10/sec) for erosion studies.

CONCLUDING REMARKS

A summary of the state of the art of predicting the penetration of semi-infinite targets by particles traveling at meteoroid velocities has been presented. From this summary it was concluded that uncertainties in predicted penetration of one order magnitude exist in the high meteoroid velocity range. Although several accurate analytical solutions of the penetration problem, treated as a hydrodynamic phenomena, have been made, uncertainties in the equation of state and the cratering criteria have caused large differences in the resulting scaling laws.

From a summary of simulation techniques it was concluded that existing devices are capable of simulating meteoroid impacts only in the lower meteoroid velocity range.
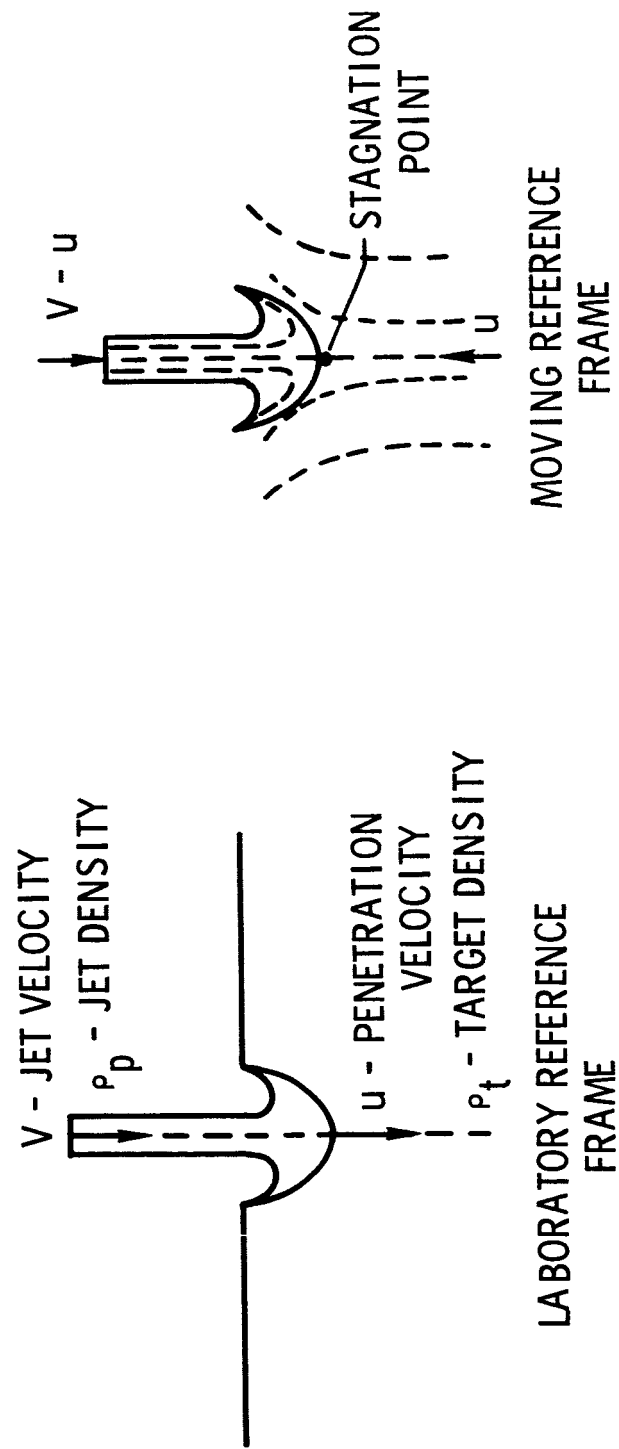
REFERENCES

1. Berkhoff, G.; MacDougall, D. P.; Pugh, E. M.; and Taylor, G. I.: Explosives With Lined Cavities. J. Appl. Phys., vol. 19, 1948.

2. Charters, A. C.: High Speed Impact. Sci. Am., vol. 203, no. 4, Oct. 1960.

3. Bjork, R. L.: Effects of a Meteoroid Impact on Steel and Aluminum in Space. Paper P-1662, The RAND Corp., Dec. 16, 1958.

4. Stanyukovich, K. P.: Concerning the Impact of Solids at High Velocities. Soviet Physics - JETP (Letters to the Editor), vol. 36(9), no. 5, Nov. 1959, p. 1141.

5. Grimminger, G.: Probability That a Meteorite Will Hit or Penetrate a Body Situated in the Vicinity of the Earth. J. Appl. Phys., vol. 19, 1948.

6. Harlow, F. H.: Particle-in-Cell Method for Numerical Solution of Problems in Fluid Dynamics. Proceedings of Symposia in Applied Mathematics, vol XV, 1963.

7. Walsh, J. M.; and Tillotson, J. H.: Hydrodynamics of Hypervelocity Impact. General Atomic Division of General Dynamics - GA-3827, Jan. 1963.

8. Vedder, James F.: Charging and Acceleration of Microparticles. The Review of Scientific Instruments, vol. 34, no. 11, Nov. 1963.

$$\text{RESISTIVE FORCE} \quad F \qquad\qquad \text{PENETRATION} \quad p/d$$

	RESISTIVE FORCE F	PENETRATION p/d
1	k	$K\left(\dfrac{\rho_p}{\rho_t}\right)V^2$
2	kp	$K\left(\dfrac{\rho_p}{\rho_t}\right)^{1/2}V$
3	kp^2	$K\left(\dfrac{\rho_p}{\rho_t}\right)^{1/3}V^{2/3}$
4	kp^2V	$K\left(\dfrac{\rho_p}{\rho_t}\right)^{1/3}V^{1/3}$
5	kp^2/V	$K\left(\dfrac{\rho_p}{\rho_t}\right)^{1/3}V$
6	$k\rho_t V^2$	$K_1\left(\dfrac{\rho_p}{\rho_t}\right)\log V + K_2$
7	$k_1\rho_t V^2 + C_2H$	$K_1\left(\dfrac{\rho_p}{\rho_t}\right)\log\left[1 + \dfrac{\rho_t V^2}{C_2H}\right]$

Figure 1.- Empirical penetration formulas.

NASA

V - u

STAGNATION
POINT

u

MOVING REFERENCE
FRAME

NASA

V - JET VELOCITY

ρ_p - JET DENSITY

u - PENETRATION
VELOCITY

ρ_t - TARGET DENSITY

LABORATORY REFERENCE
FRAME

Figure 2.- Penetration by jet action.
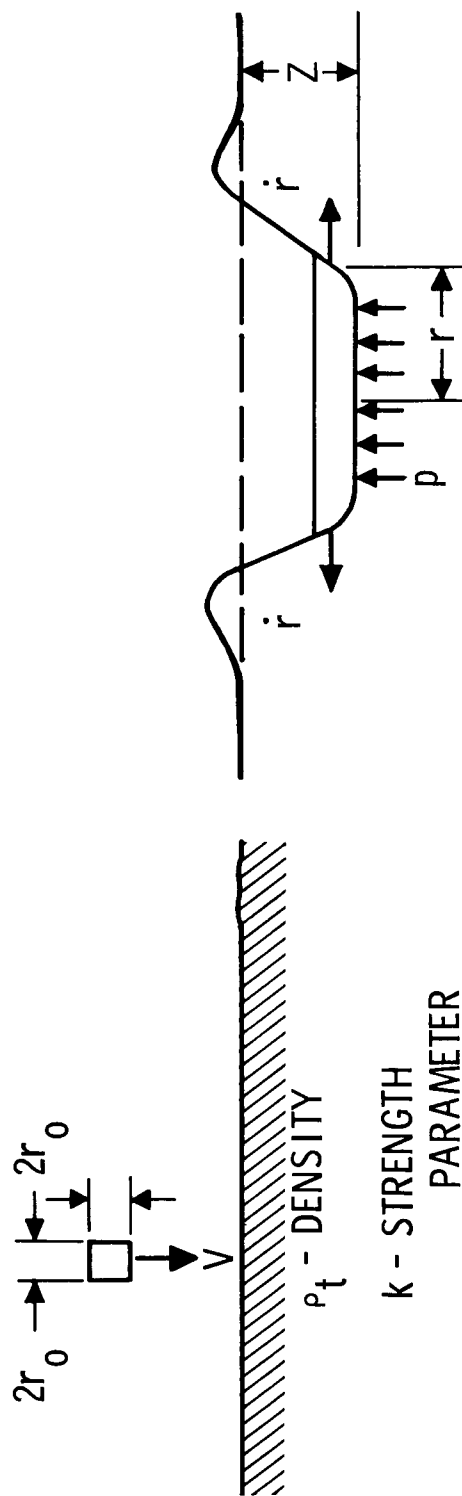
Figure 3.- Öpik's description of crater formation.
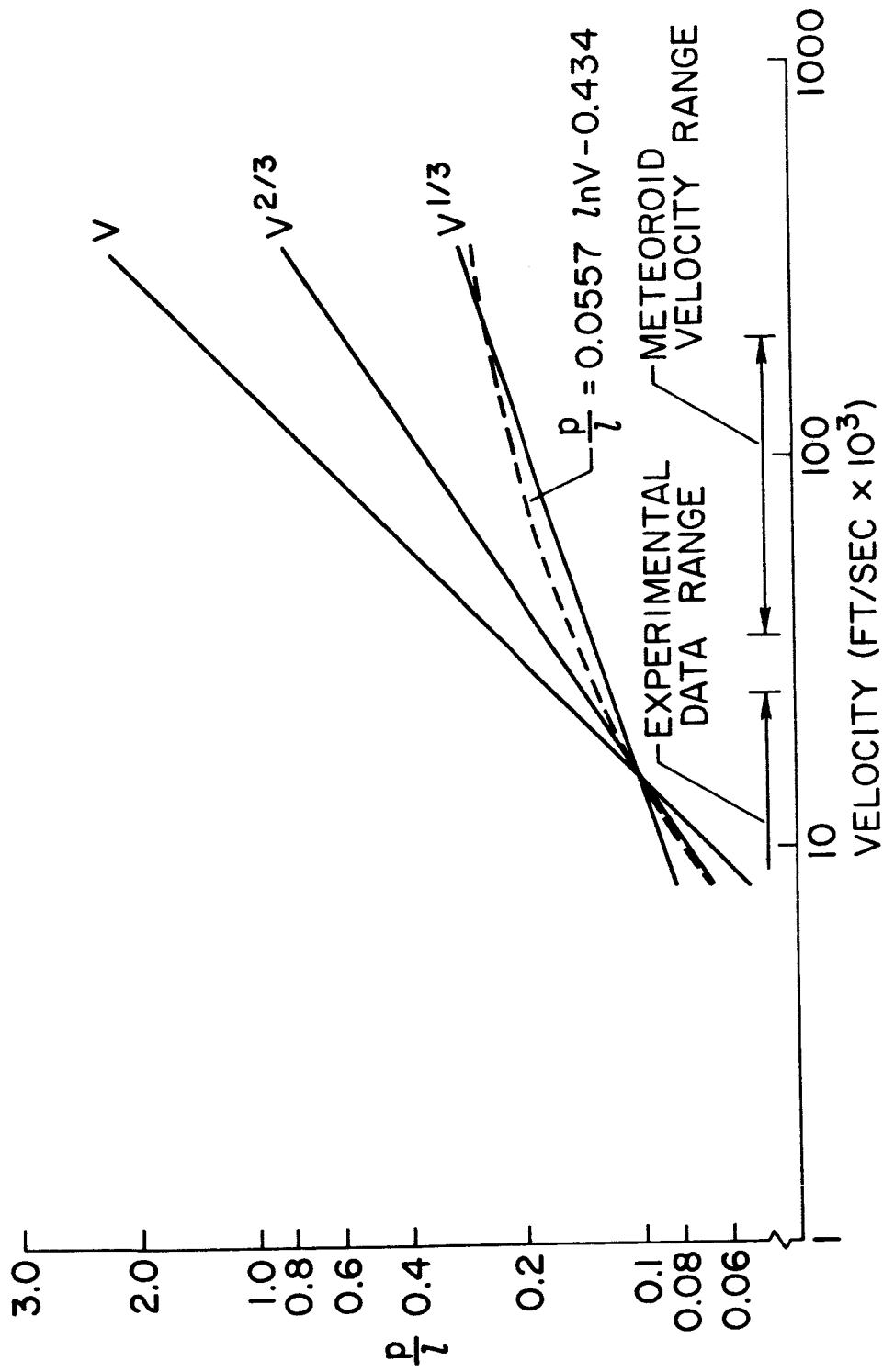
Figure 4.- Empirical penetration curves.

NASA

REGION I - PROJECTILE REMAINS INTACT $\left(P \sim V^{4/3}\right)$

REGION II - PROJECTILE DEFORMS AND SHATTERS

REGION III - FLUID IMPACT $\left(P \sim V^{2/3}\right)$
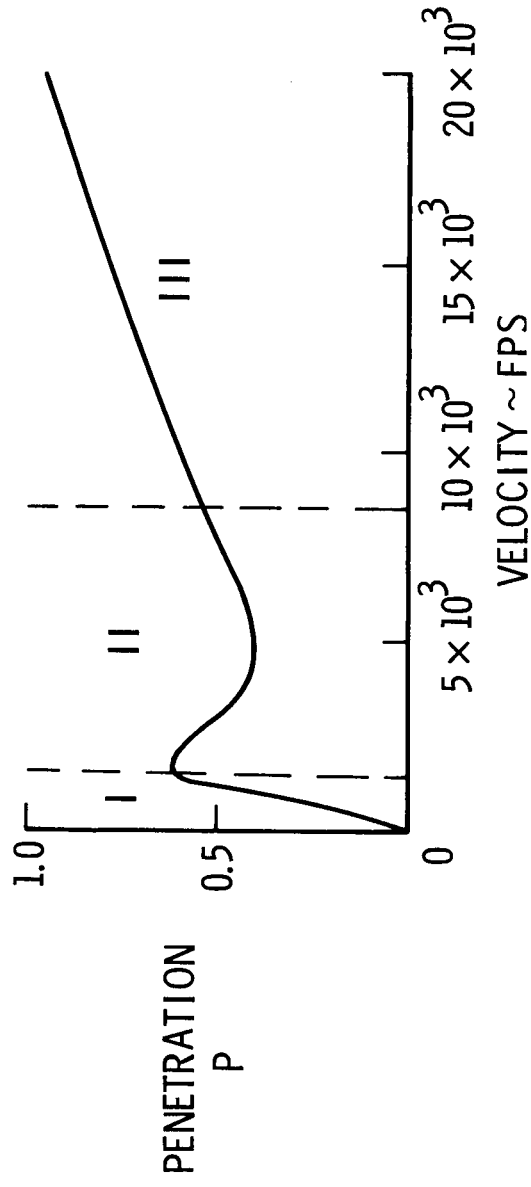
NASA

Figure 5.- Impact of steel and tungsten carbide into soft lead.
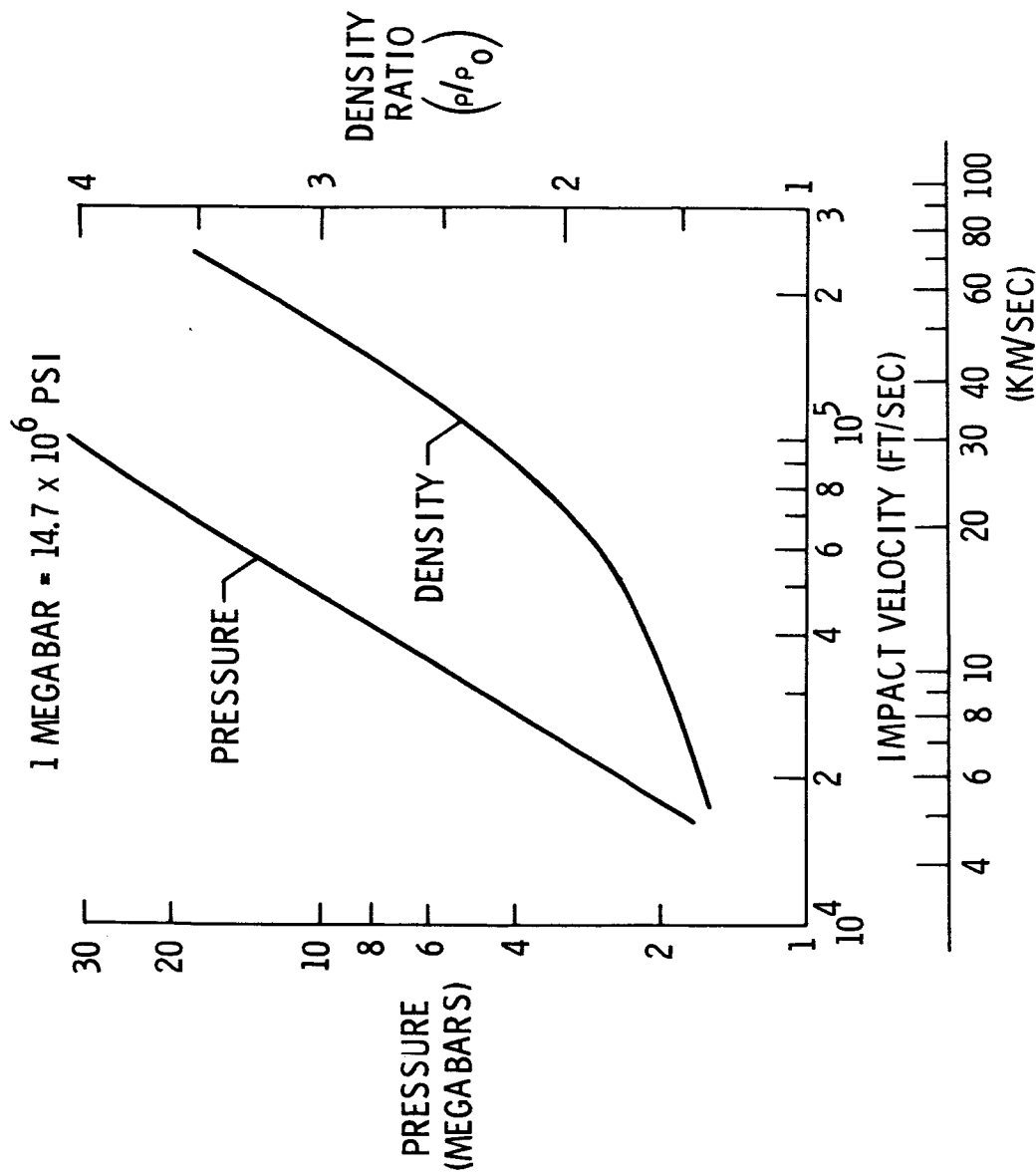
Figure 8.- One-dimensional shock conditions for iron.

NASA

THERMAL PENETRATION

$$\frac{p}{d} = K\left(\frac{\rho_p}{\rho_t}\right)^{1/3} \frac{V^{2/3}}{Q^{1/3}}$$

EXPLOSIVE PENETRATION

$$\frac{p}{d} = K\left(\frac{\rho_p}{\rho_t}\right)^{1/3} \frac{V^{2/3}}{R^{1/3}}$$

GRIMMINGER'S HYDRODYNAMIC PENETRATION

$$\frac{p}{d} = \frac{4}{3} \frac{\rho_p}{\rho_t} \ln \frac{V}{5C} + \frac{25C^2}{3} \frac{\rho_p}{K}$$

$$K = 5.03 \frac{\sigma_t}{\sigma_{CU}} \times 10^7$$

C – PLASTIC WAVE VELOCITY

Figure 9.- Theoretical penetration equations.
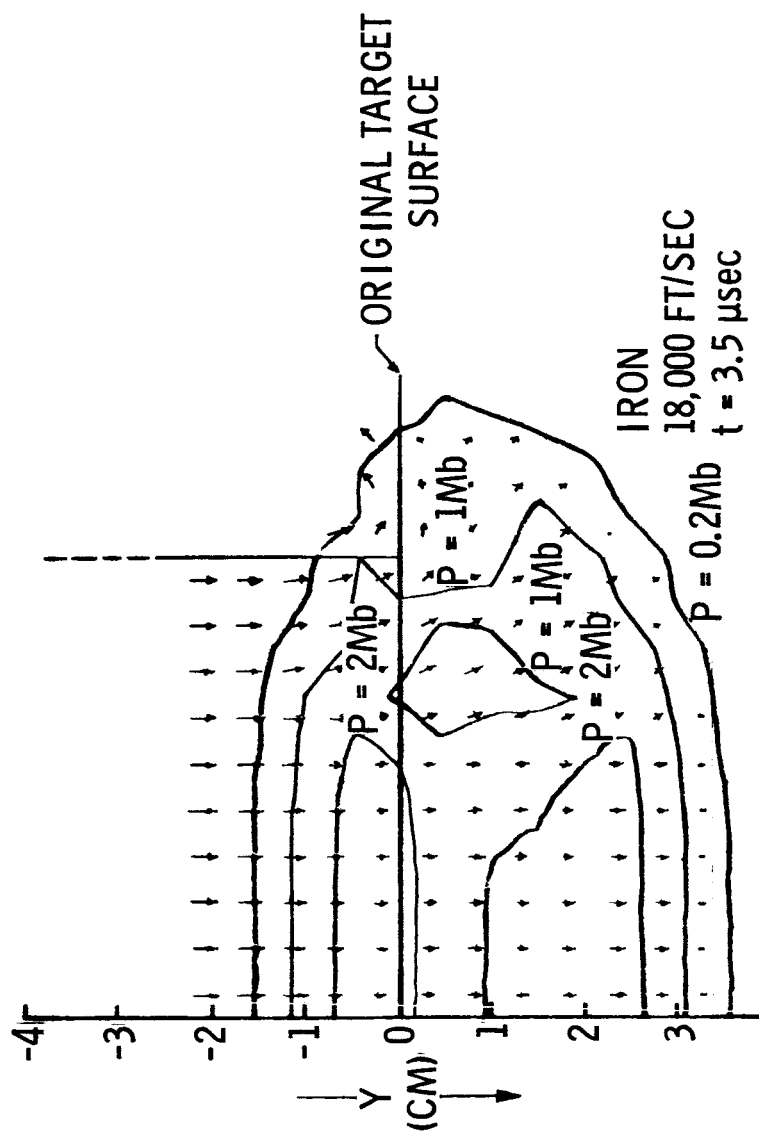
Figure 10.- Pressure contours and velocity field.
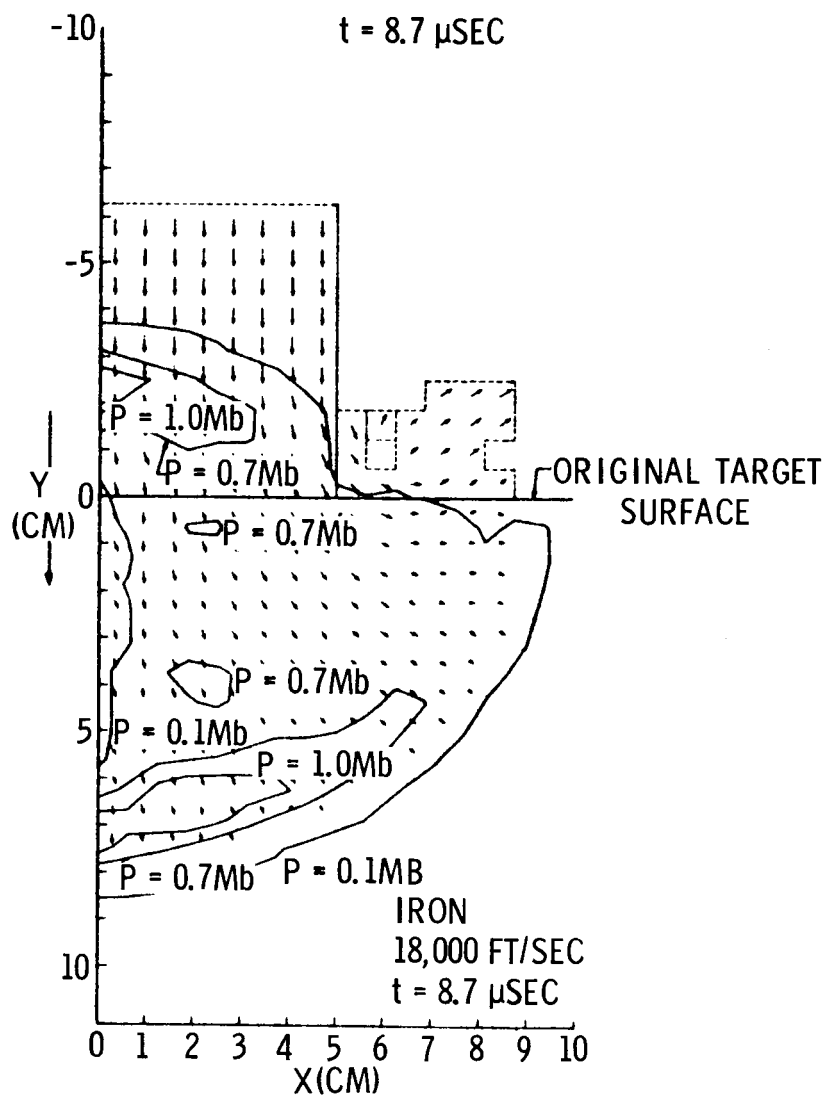
Figure 11.- Pressure contours and velocity field.
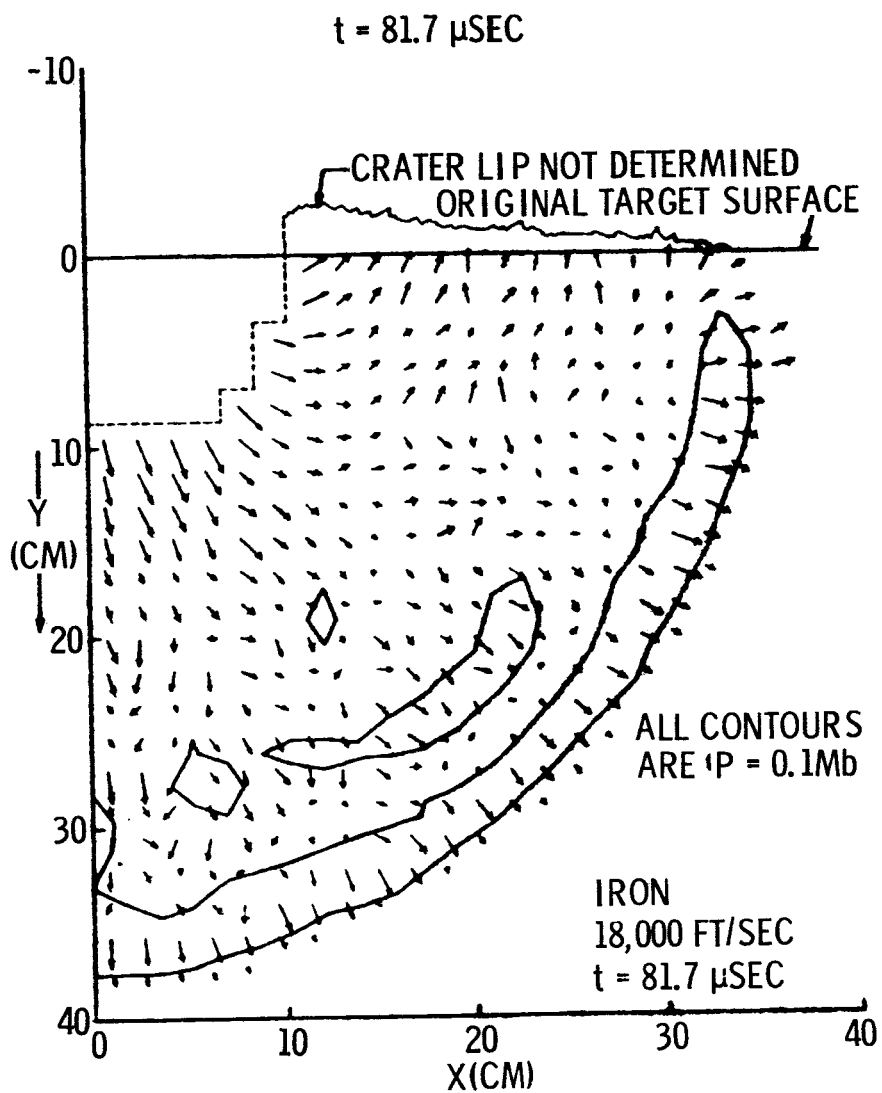
Figure 12.- Pressure contours and velocity field.
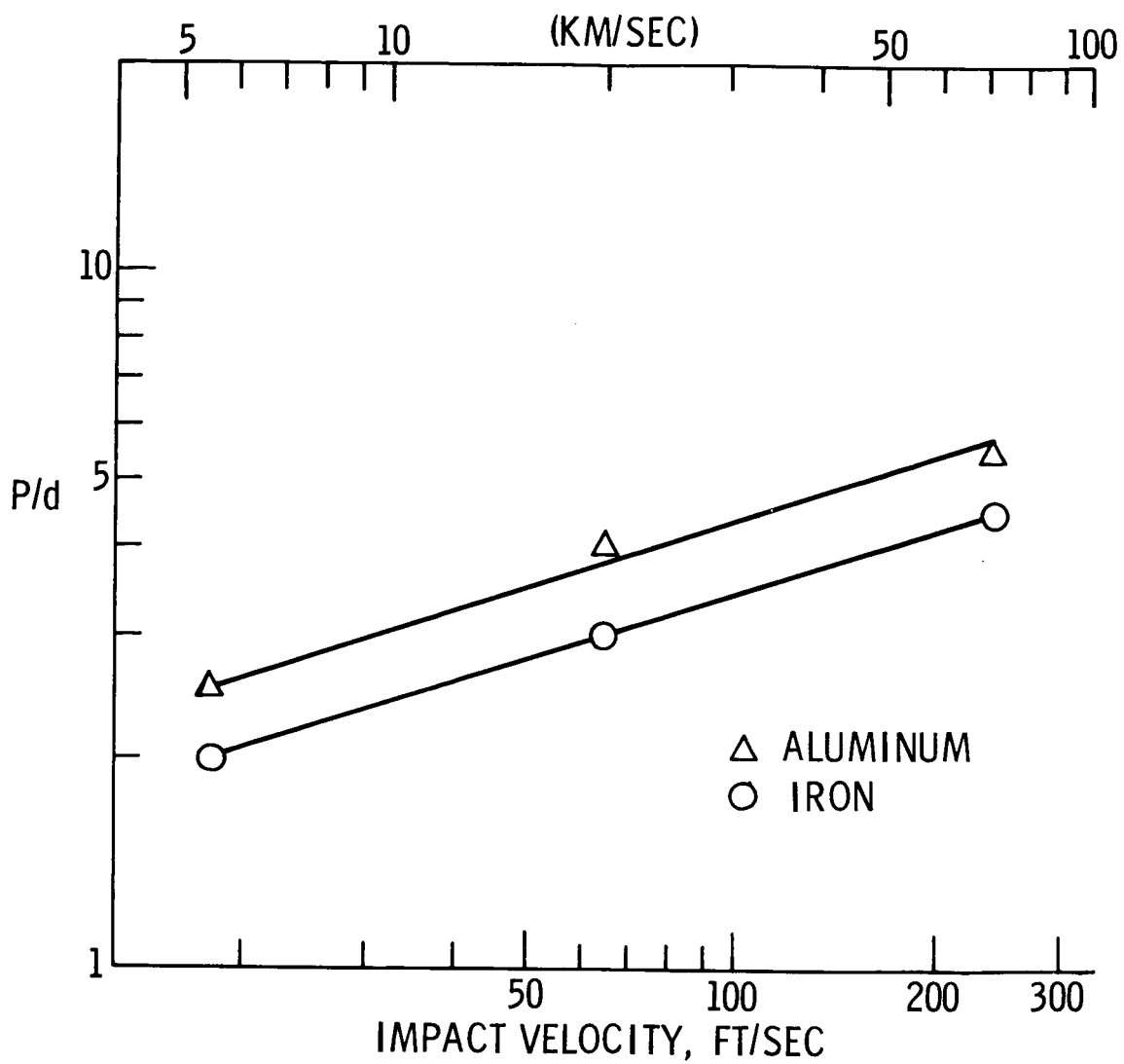
Figure 13.- Bjork's penetration results.
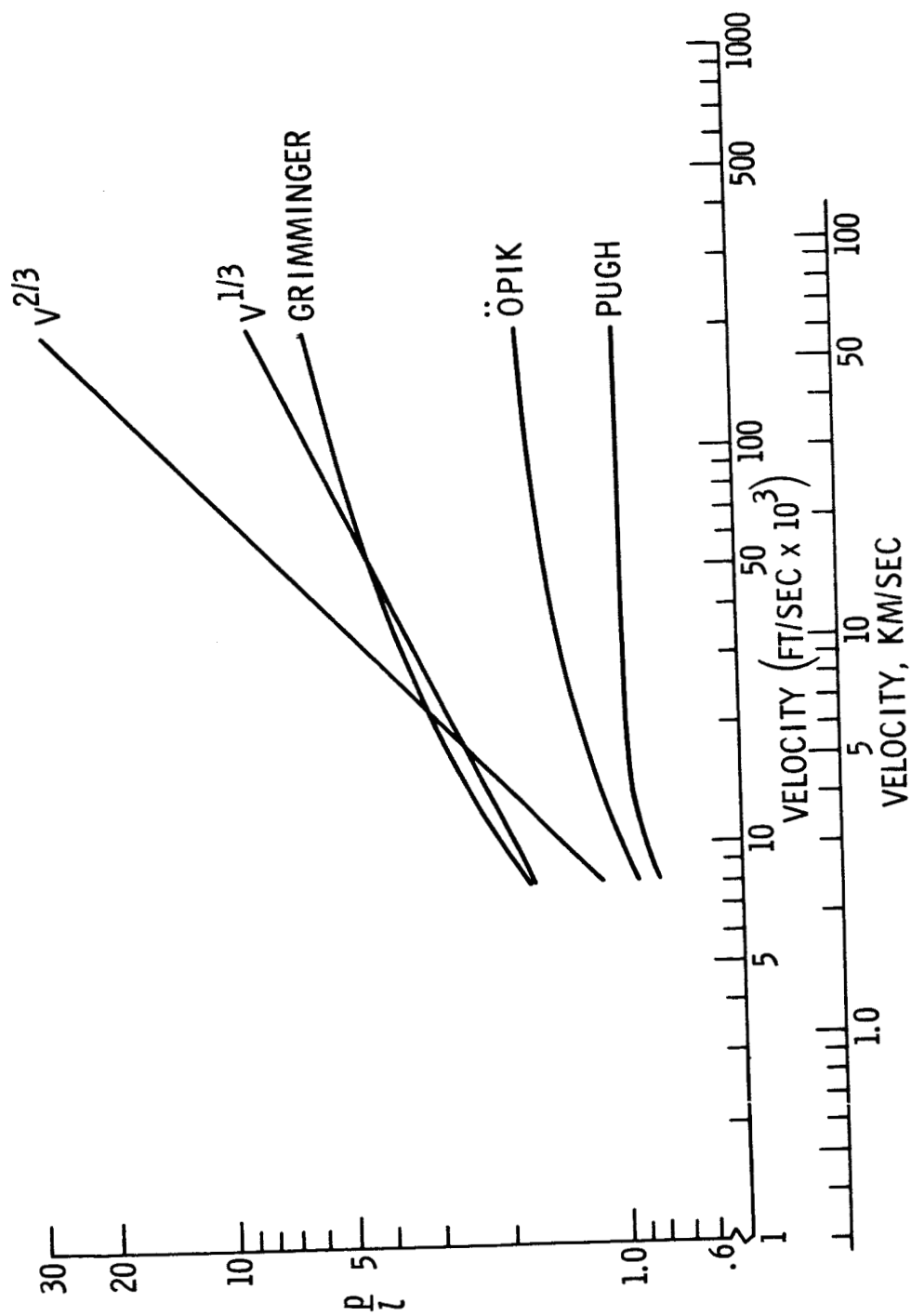
NASA

Figure 14.- Theoretical penetration curves.
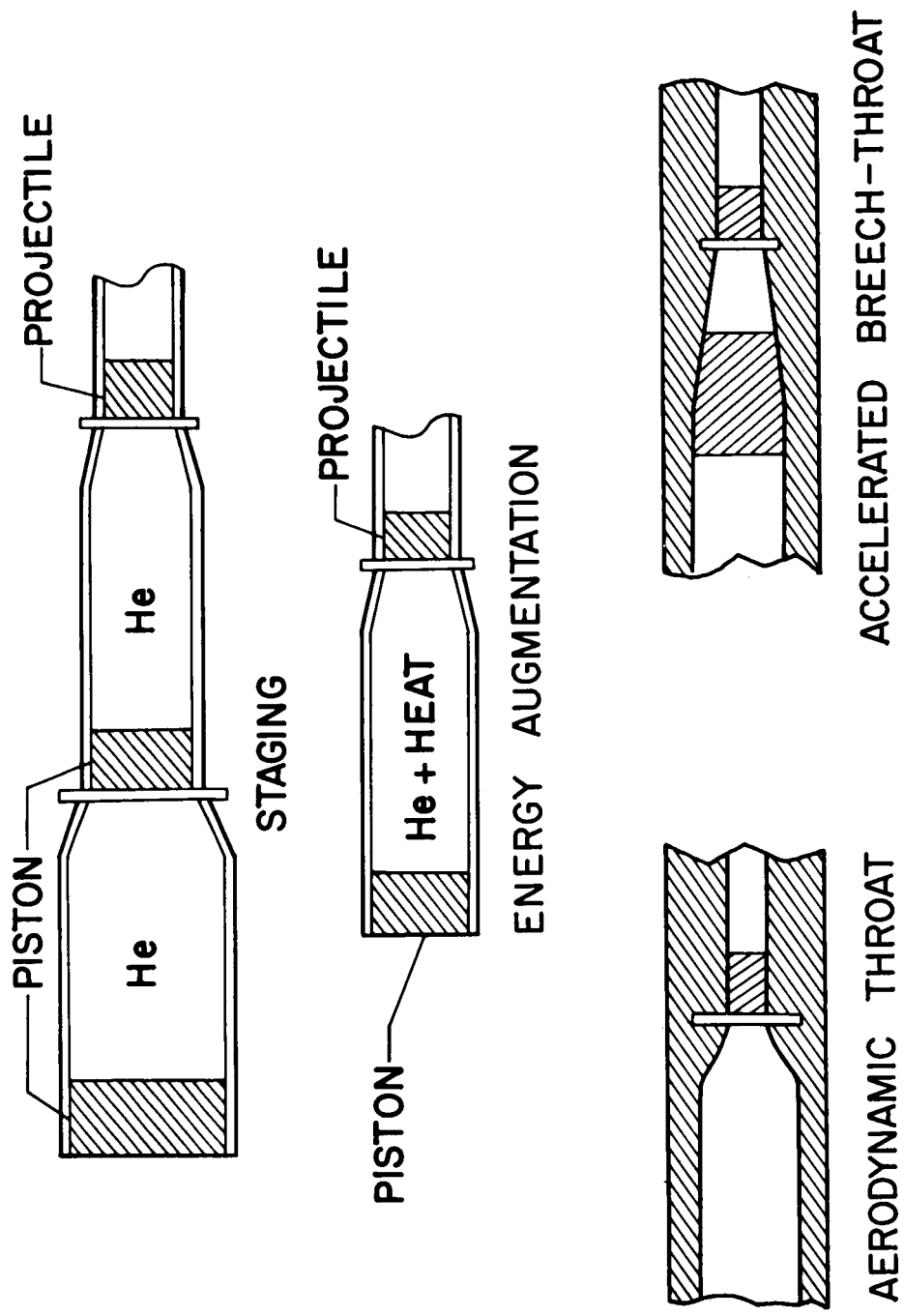
NASA

Figure 15.- Modified light-gas gun techniques.
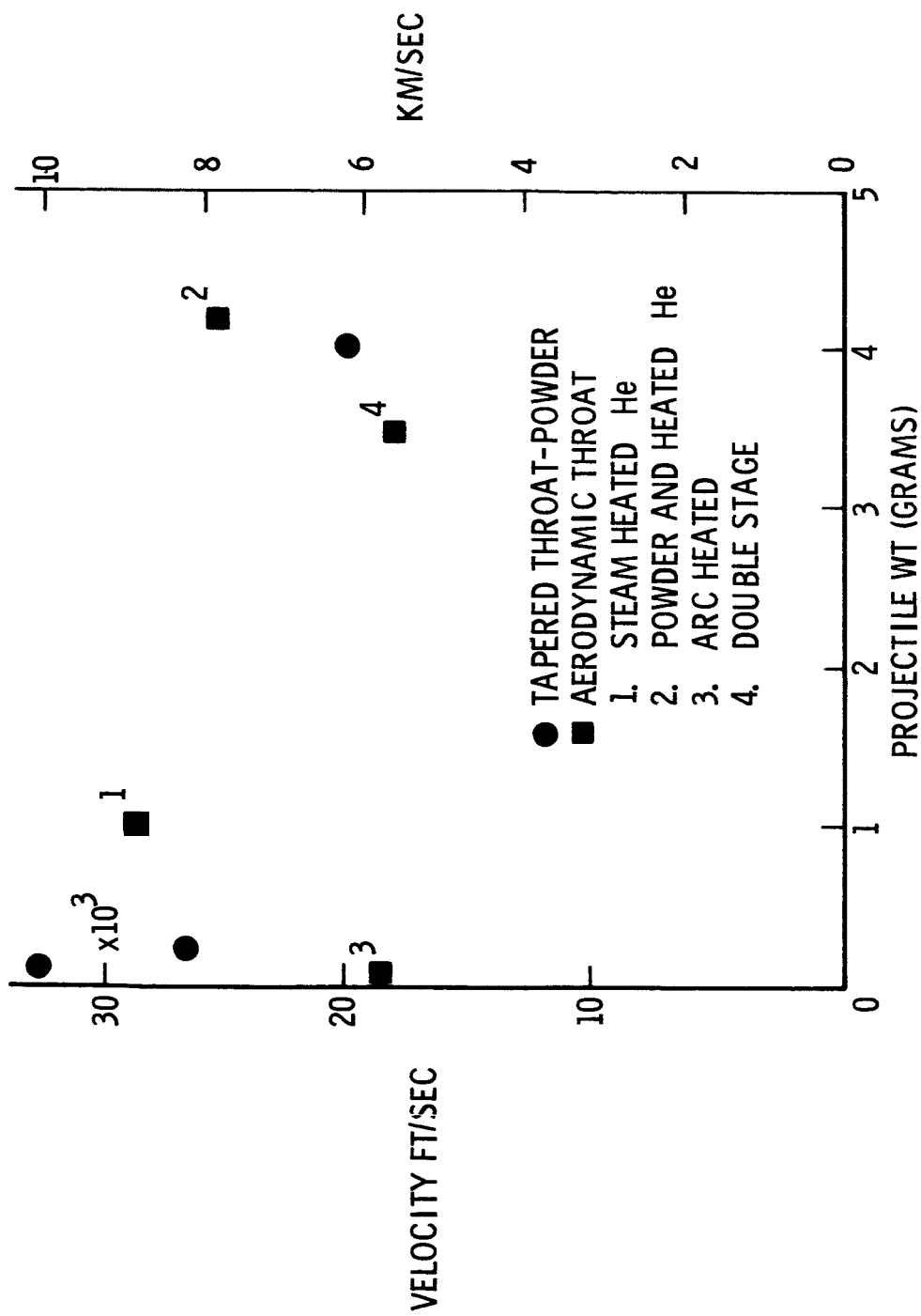
Figure 16.- Light-gas gun capabilities.
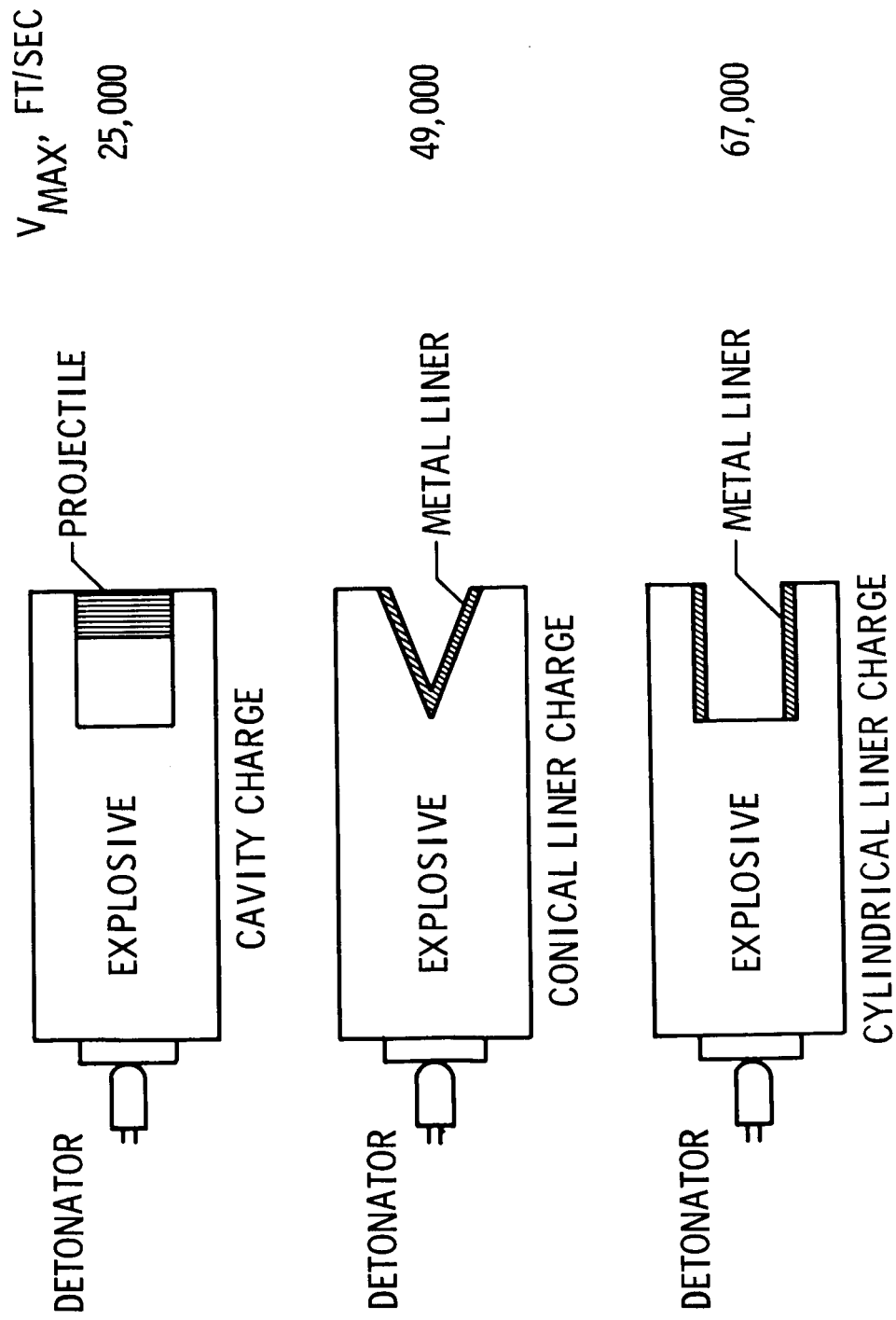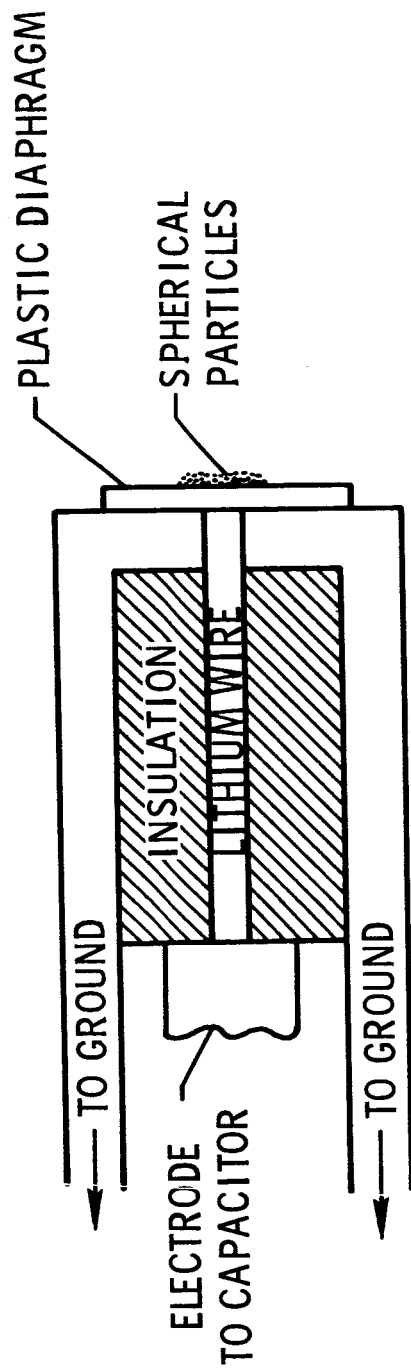
Figure 17.- Modified shaped-charge techniques.
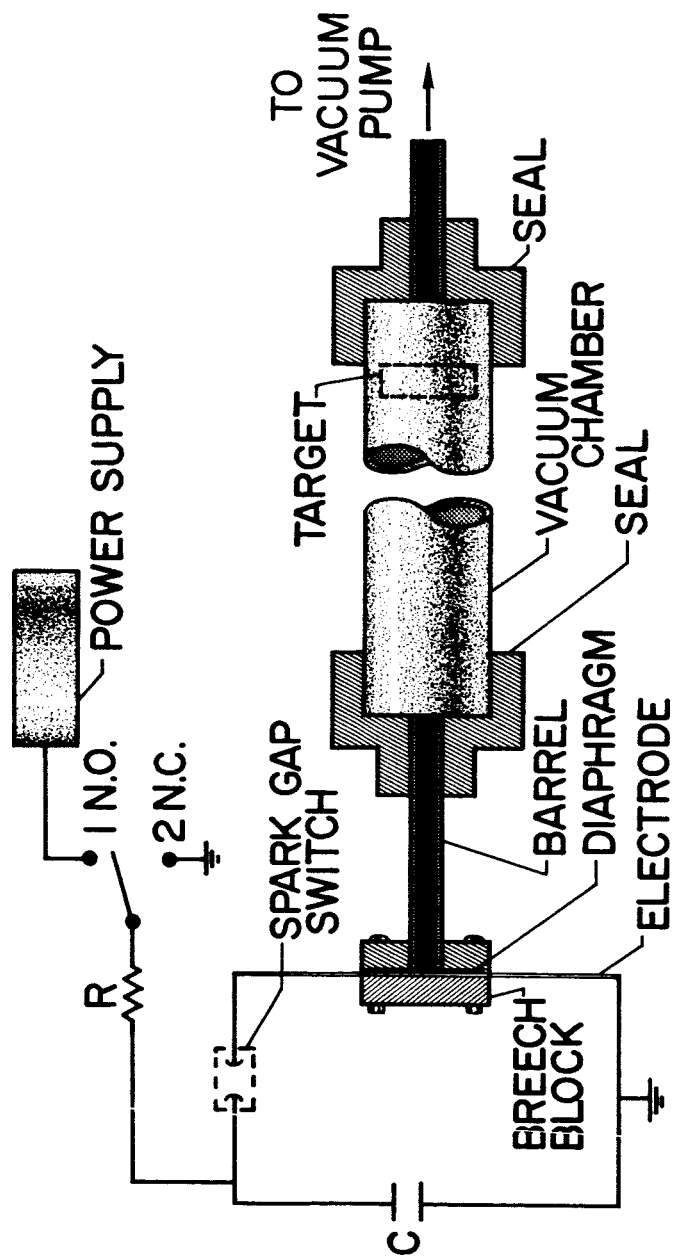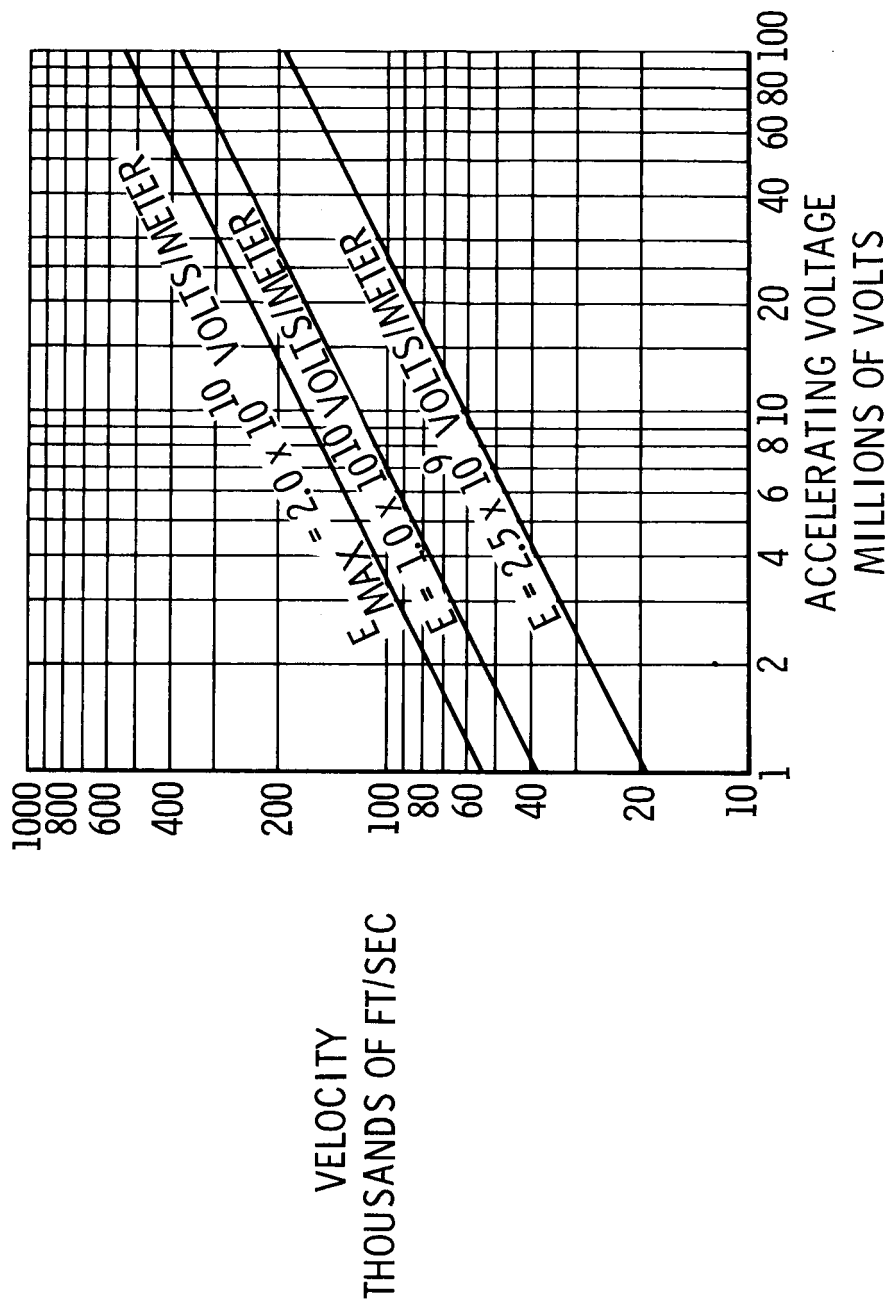
Figure 18.- Exploding foil gun facility schematic.

NASA

10 μ SEC   25 μ SEC   28 μ SEC   30 μ SEC
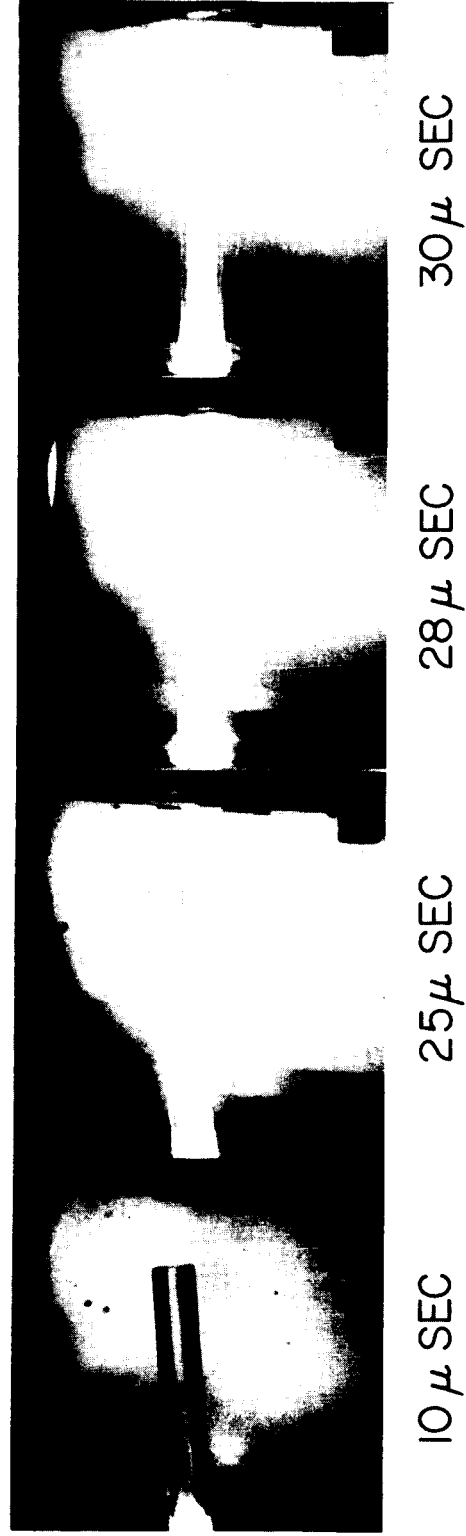
NASA

Figure 19.- The exploding foil gun firing sequence.

PLASTIC DIAPHRAGM

SPHERICAL
PARTICLES

INSULATION

LITHIUM WIRE

TO GROUND

TO GROUND

ELECTRODE
TO CAPACITOR

NASA

Figure 20.- N.A. exploding wire gun.

Figure 21.- Velocity versus voltage for 1-micron iron particles.

NASA

(SLOAN-LAWRENCE)
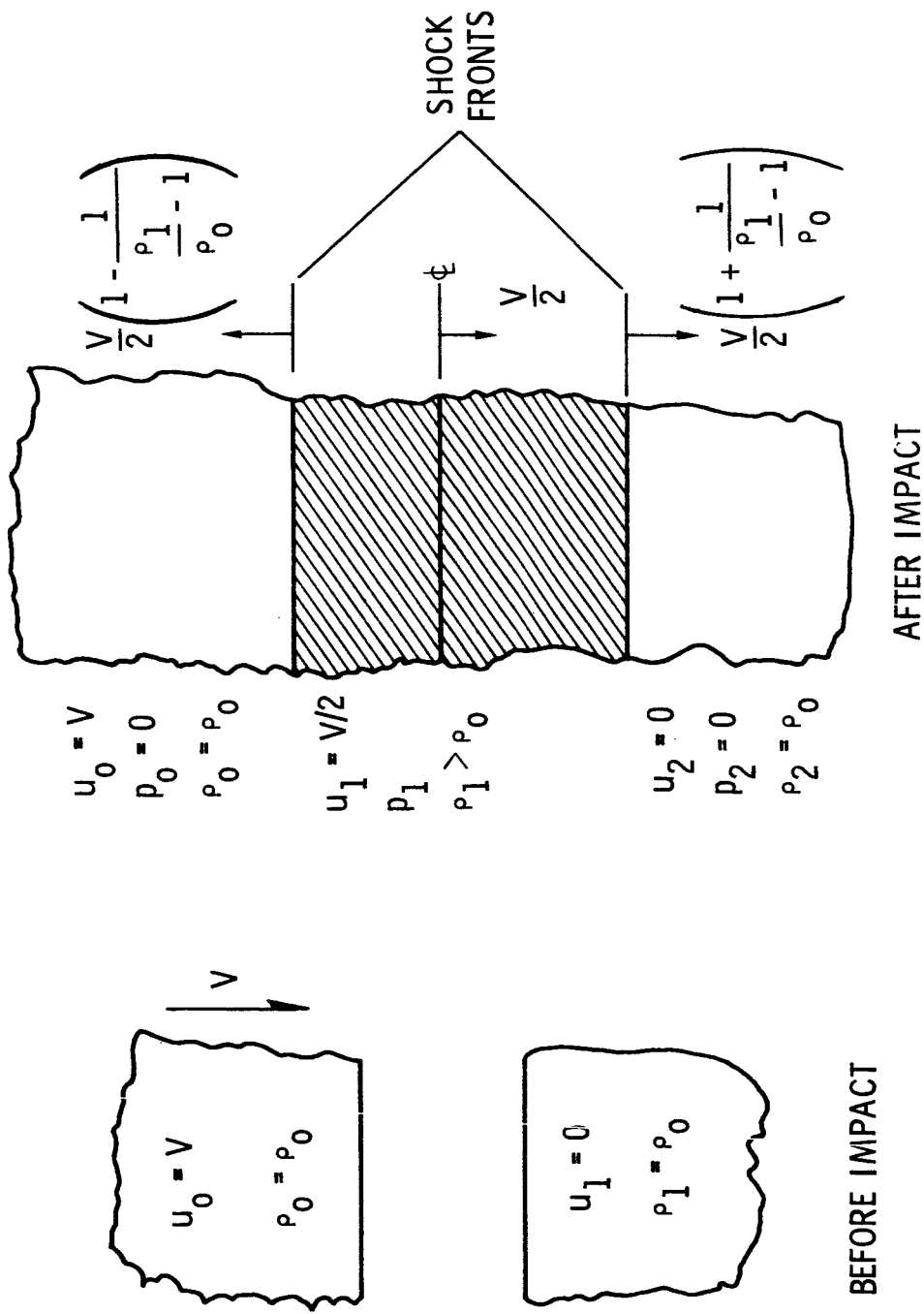
CYLINDRICAL DRIFT TUBES

BUS BARS

A. C. POWER SOURCES
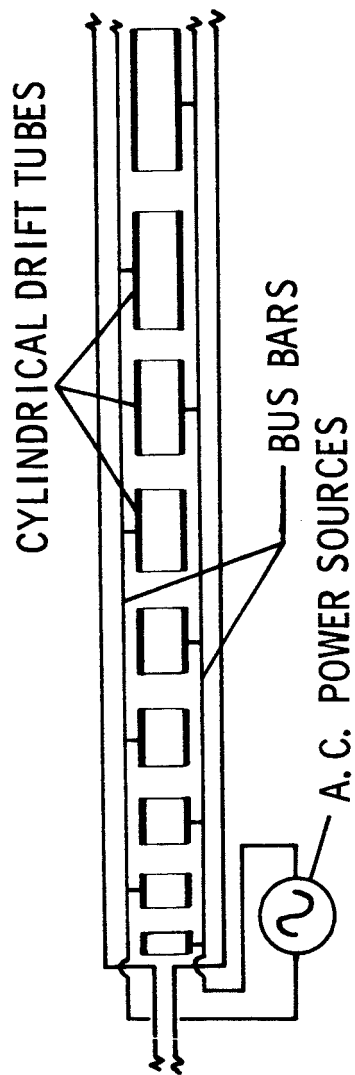
NASA

Figure 22.- Linear accelerator.
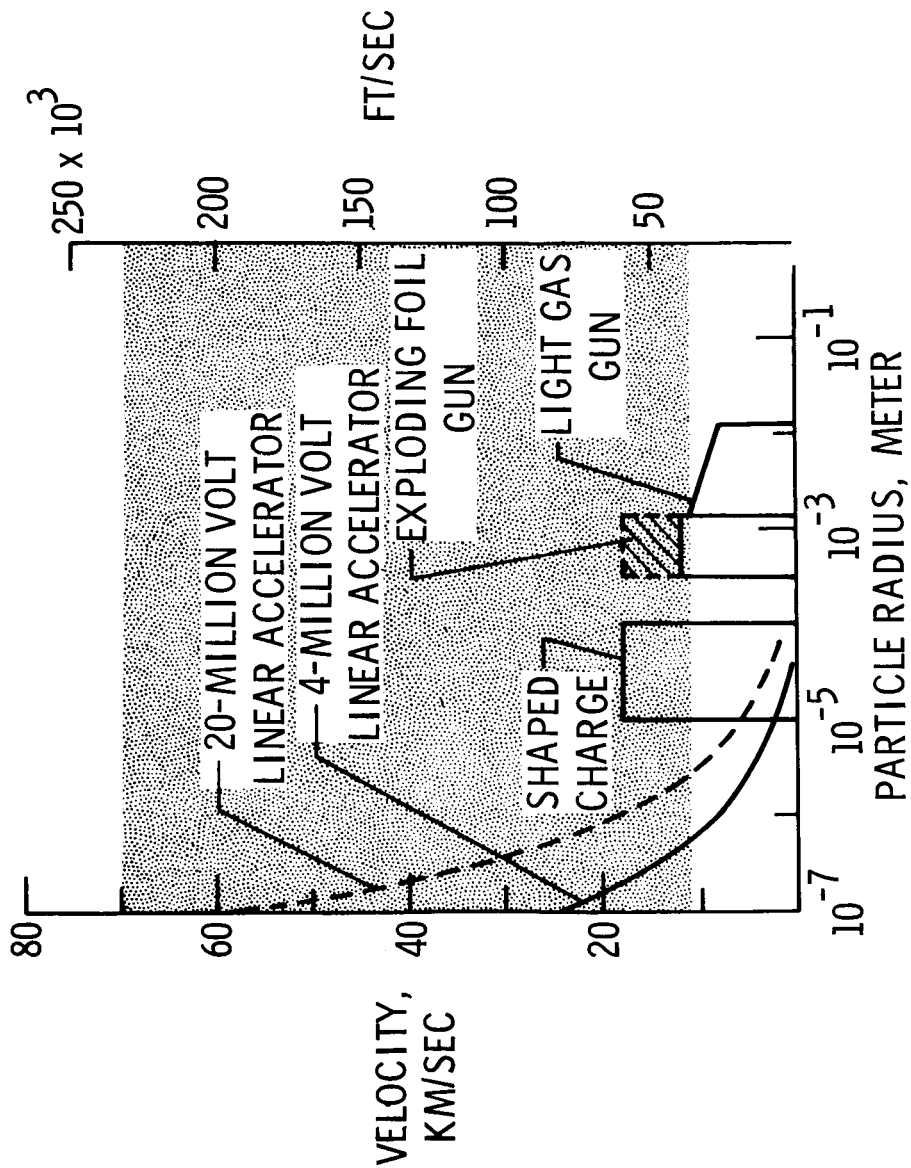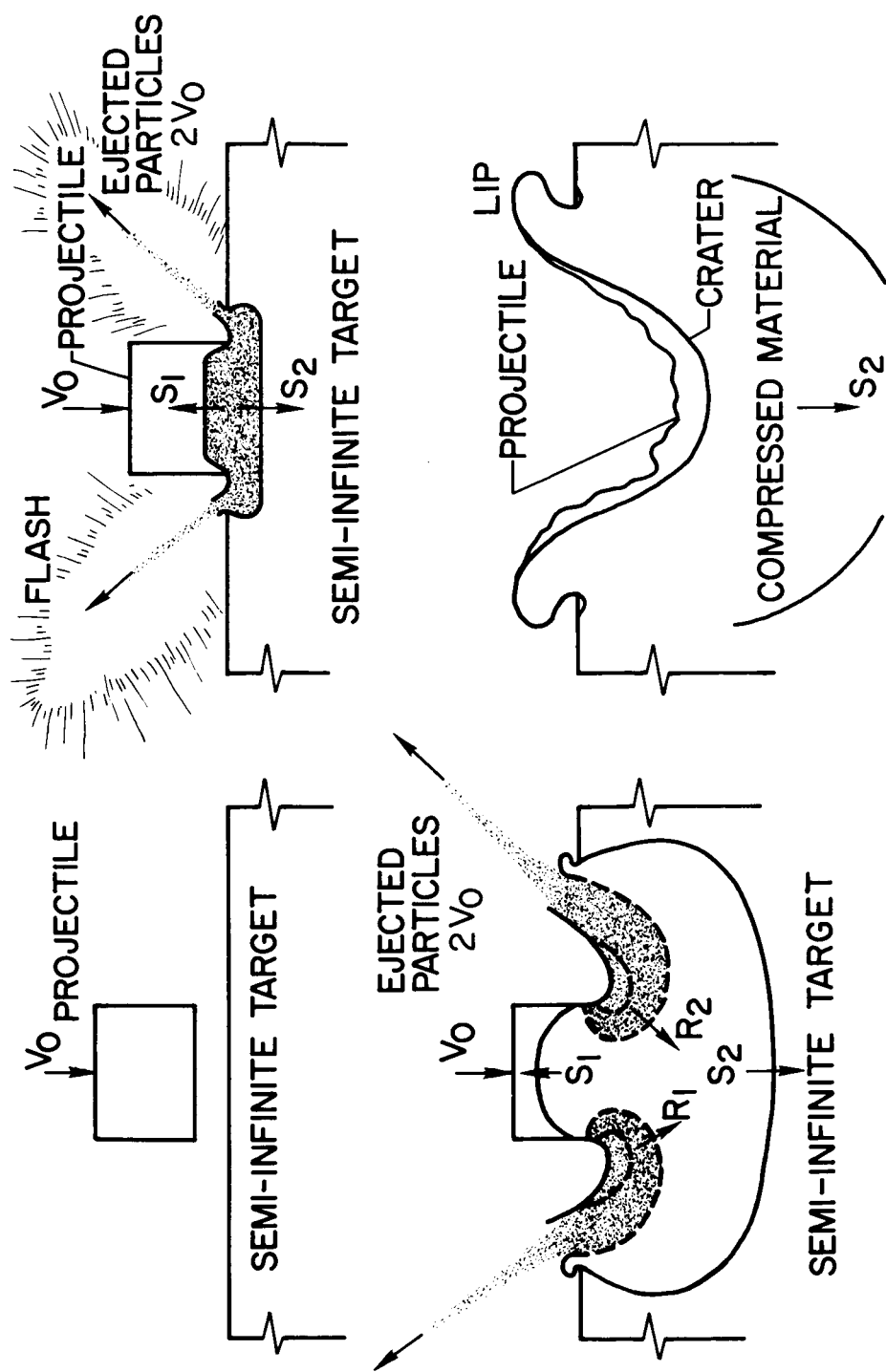
Figure 23.- Summary of meteoroid simulation techniques.

Figure 7.- One-dimensional impact.

NASA

Figure 6.- Impact mechanism.

NASA